Relationship Between Active and Passive Microwave Signals Over Vegetated Surfaces

Moritz Link, Thomas Jagdhuber, *Senior Member, IEEE*, Paolo Ferrazzoli, *Senior Member, IEEE*, Leila Guerriero, *Member, IEEE*, and Dara Entekhabi, *Fellow, IEEE*

***Abstract*— The NASA Soil Moisture Active Passive (SMAP) satellite mission aims to produce enhanced resolution surface soil moisture products by combining coincident but multiresolution L-band active and passive microwave measurements. Since the SMAP radar ceased operations early in the mission, Copernicus Sentinel-1 C-band radar observations are used in the combined product. The synergy is built on two basic foundations: first, active and passive signals covary in a known and systematic fashion, and second, measurements are available at multiple resolutions. In this study, we perform numerical simulations and assess global satellite observations to test the first foundation (covariation). Specific focus lies on the role of the vegetation canopy in modulating the active–passive relationship. We use a discrete radiative transfer model to simulate the slope β and coefficient of determination R^2 of the relationship between active and passive signals, considering three vegetation types for which the model has been extensively assessed in previous experimental studies. We find that a linear relationship between backscatter and emissivity can be established over a range of vegetation conditions. The coupling between active and passive signals decreases with increasing vegetation water content, such that moderate or higher correlations (nonzero slopes) are retained up to 4 kg/m^2 (6.3 kg/m^2) for L-band/L-band and 1.5 kg/m^2 (2 kg/m^2) for the C-band/L-band configuration. We decompose the effects of different soil-vegetation scattering mechanisms, such as double-bounce, and different measurement error levels on the active–passive relationship. Comparisons with satellite data confirm that our simulations capture magnitudes and major trends found across global vegetated land masses.**

***Index Terms*— Active–passive microwave sensing, soil moisture, vegetation.**

I. Introduction

SATELLITE-BASED microwave instruments enable the global monitoring of surface soil moisture, a key parameter for determining water, carbon, and energy fluxes between land and the overlying atmosphere. These exchanges are relevant to a broad range of applications, including weather prediction, climate analysis, flood forecasting, and drought monitoring [1]–[8]. In the microwave, two instrument types are commonly distinguished: Passive instruments show a high sensitivity to soil moisture, but spatial resolutions typically to not exceed tens of kilometers. Active instruments enable subkilometer spatial resolutions but are more sensitive to scattering effects from vegetation and soil surface roughness. The Soil Moisture Active Passive (SMAP) mission, launched in 2015, aims to combine the relative strengths of both instrument types [1]. Particularly, SMAP carries an L-band synthetic aperture radar (SAR) to disaggregate coincident L-band radiometer observations for an intermediate resolution soil moisture product [9] (see [10], [11] for reviews of existing downscaling techniques). Since a malfunction caused the active instrument to stop operations in July 2015, the Sentinel-1 C-band SAR was chosen as substitution [12], [13].

The SMAP synergistic approach is dependent on two main factors: first, active and passive measurements covary in a known and systematic fashion, and second, the signals are available at multiple resolutions. In this study, we investigate the first of these two factors by analyzing the slope (β) and coefficient of determination (R^2) of the linear relationship between active and passive measurements. The slope β serves as a critical algorithm parameter and is one of the main uncertainty sources in the SMAP downscaling procedure [12], [14]. Previous studies found a dependence between β and local vegetation cover conditions [15]–[21], which is in line with theoretical expectations [13]. However, slope estimates from observational data can be affected by rapidly changing vegetation and soil roughness conditions [19], [20], subpixel land cover heterogeneity [21]–[26], or biases induced by measurement errors [27]. In addition, only few studies investigated the active–passive slope and coefficient of determination when higher frequency radar signatures in C-band are considered [27]–[30]. Previous simulation studies assessed the slope only for limited vegetation type conditions [31] or using simplified physical models that ignore higher order scattering effects [32]. No previous simulation studies investigate vegetation type diversity, the combination of L-band radiometer and C-band radar signatures, or measurement error effects.

In this study, we use numerical simulations and global satellite observations to assess the relationship between active and passive microwave signatures over vegetated surfaces. We ask: How is the relationship of active and passive signals from

Manuscript received July 13, 2020; revised December 9, 2020; accepted January 16, 2021. Date of publication November 30, 2021; date of current version January 26, 2022. This work was supported in part by the Massachusetts Institute of Technology (MIT)–Germany MIT International Science and Technology Initiatives program. *(Corresponding author: Moritz Link.)*

Moritz Link is with the German Aerospace Center (DLR), Microwaves and Radar Institute, 82234 Wessling, Germany, and also with the Department of Geography, Ludwig-Maximilians University of Munich, 80333 Munich, Germany (e-mail: moritzlink0@gmail.com).

Thomas Jagdhuber is with the German Aerospace Center (DLR), Microwaves and Radar Institute, 82234 Wessling, Germany, and also with the Institute of Geography, University of Augsburg, 86159 Augsburg, Germany.

Paolo Ferrazzoli and Leila Guerriero are with the University of Rome Tor Vergata, Dipartimento di Ingegneria Civile e Ingegneria Informatica, 00133 Rome, Italy.

Dara Entekhabi is with the Department of Civil and Environmental Engineering, Massachusetts Institute of Technology, Cambridge, MA 02139 USA.

Digital Object Identifier 10.1109/TGRS.2021.3053586

rough surfaces affected by the density of the overlying vegetation cover? Over what range of vegetation density can both measurements be usefully combined? We assess these questions for the SMAP (L-band radar and radiometer) and novel Sentinel-1 and SMAP (C-band radar and L-band radiometer) frequency configurations. The analysis therefore applies to the evaluation of the SMAP combined active–passive soil moisture products [9], [12]. The study is structured as follows: Analytical formulations for the active–passive slope and coefficient of the determination in the presence of measurement noise are developed in Section II. Backscatter and emissivity signatures for three vegetation types are simulated using a discrete radiative transfer model described in Section III. Simulations are assessed using satellite observations described in Section IV. The results are discussed and conclusions are summarized in Sections V and VI, respectively.

II. Relationship Between Active and Passive Microwave Signatures

Active and passive microwave observations over land are sensitive to geophysical parameters such as surface soil moisture, soil surface roughness, and vegetation cover. These variables change on different timescales: for short observation periods like hours or days, vegetation and soil roughness conditions are often considered quasi-constant, while soil moisture can show significant variability due to wetting and dry down events [33]–[35]. In this case, the backscatter coefficient σ^0 and emissivity e exhibit opposite responses to changes in soil moisture, that is, the backscatter coefficient increases while the emissivity decreases for increasing soil moisture (and vice versa). A hypothesis was consequently stated in [36] that, given the above conditions, backscatter and emissivity follow a linear functional relationship

$$e = \alpha + \beta\sigma^0 \tag{1}$$

where α and β are the intercept and slope parameters, respectively. We investigate the relationship for linear unit backscatter in accordance with the current SMAP algorithm version [12]. Backscatter coefficients in this study are in linear units unless otherwise stated.

A. Measurement Error Model

The backscatter and emissivity terms in (1) are subject to errors when derived from radar and radiometer measurements. This can weaken the linear relationship and introduce biases on the intercept and slope parameters. To account for these effects, we model backscatter and emissivity as two components: the first component represents the geophysical signal, assumed to be driven by changes in soil moisture θ, and the second component represents measurement noise

$$\sigma^0 = \sigma^0_\theta + \eta \tag{2}$$

$$e = e_\theta + \nu \tag{3}$$

where all terms are random variables and η and ν are zero mean random terms in backscatter and emissivity units, respectively, assumed to be uncorrelated with each other and with the geophysical signal (i.e., all respective covariances are zero). Note that backscatter measurements follow multiplicative error statistics; however, as we show in the Appendix, such errors can be represented through the additive formulation above while retaining the same error assumptions. The resulting relationship is

$$(e_\theta + \nu) = \alpha + \beta\left(\sigma^0_\theta + \eta\right) + \varepsilon \tag{4}$$

where ε is a random residual term in emissivity units. Based on (4), analytical formulations for the active–passive slope and coefficient of determination are derived in the following.

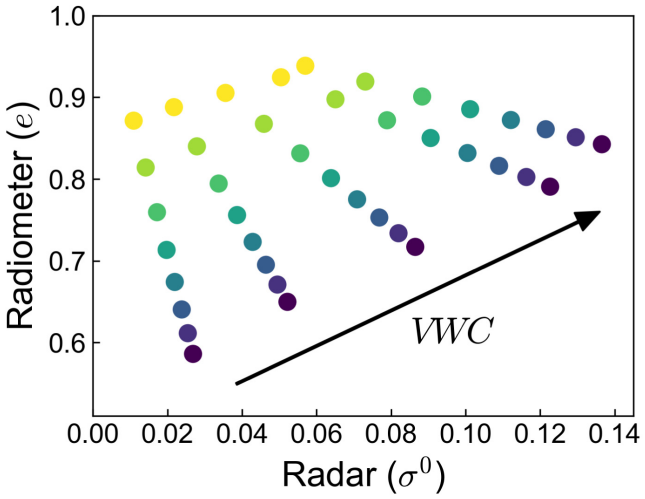

Fig. 1. Linear relationship between backscatter and emissivity due to changes in surface soil moisture (TVM simulations, yellow through blue indicates soil moisture contents of 0.05–0.40 m^3m^{-3}). The dependence on the vegetation water content is indicated for an example case of corn, H-polarization and L/L-band configuration. Note that the decrease in the slope with increasing vegetation water content is inherent to the chosen example (see Fig. 4 for all other cases). The slope of the error-free relationship, shown here, is referred to as β_θ in this study.

B. Slope β

The least-squares slope of the relationship in (4) is given by

$$\beta = \frac{Cov\left(\sigma^0_\theta + \eta, e_\theta + \nu\right)}{Var\left(\sigma^0_\theta + \eta\right)} \tag{5}$$

with $Cov(\cdot)$ and $Var(\cdot)$ denoting covariances and variances, respectively. From the error term assumptions, (5) can be simplified to

$$\beta = \frac{Cov\left(\sigma^0_\theta, e_\theta\right)}{Var\left(\sigma^0_\theta\right) + Var\left(\eta\right)} = \beta_\theta \frac{Var\left(\sigma^0_\theta\right)}{Var\left(\sigma^0_\theta\right) + Var\left(\eta\right)} \tag{6}$$

where $\beta_\theta = Cov(\sigma^0_\theta, e_\theta)/Var(\sigma^0_\theta)$ is the slope of the error-free relationship, illustrated through example simulations in Fig. 1. We can express β conceptually as the product $\beta = \beta_\theta B$, where $B = Var\left(\sigma^0_\theta\right)/[Var\left(\sigma^0_\theta\right) + Var\left(\eta\right)]$ is a bias factor taking values between zero and unity. It follows that the slope of the relationship observed with errors, β, is generally smaller in magnitude than the slope of the underlying relationship, β_θ. This well-established effect,

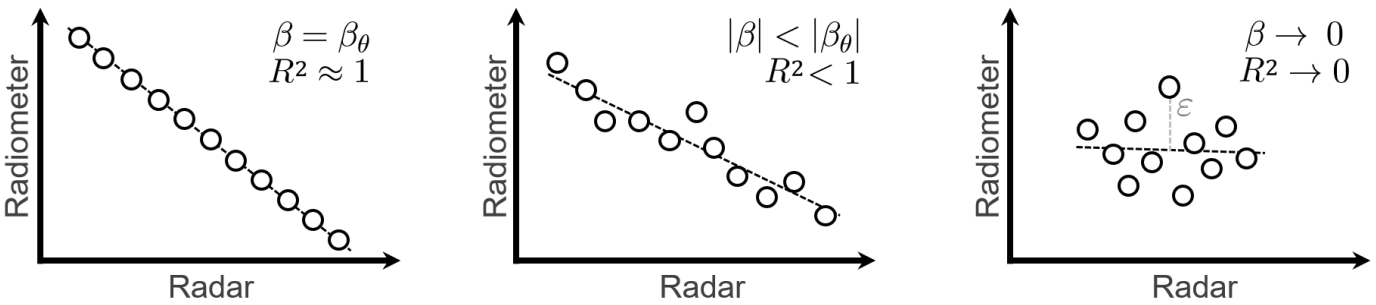

Fig. 2. Impact of measurement errors on the active–passive relationship. (Left) Underlying relationship due to changes in surface soil moisture. (Middle) Same relationship observed with errors. The slope is biased towards lower magnitudes and the coefficient of determination is weakened. Slope biases occur only in the presence of radar measurement errors. (Right) Same relationship for high errors or low soil moisture sensitivities (constant soil moisture variability assumed, axis limits may vary). The slope and coefficient of determination approach zero. The residual ε is indicated.

often referred to as "attenuation" in linear regression [37], results from the residuals ε being minimized in the emissivity direction. A schematic illustration is provided in Fig. 2. Notice that the bias depends solely on errors of the backscatter term or, more specifically, the ratio of its signal and error variances.

For further decomposition of the above expressions, we introduce the assumption of linear backscatter and emissivity soil moisture sensitivities. Possible approximation errors of this assumption are discussed in Section II-D. Given linear sensitivities, the error-free slope can be written as

$$\beta_\theta = \frac{E}{S} \tag{7}$$

where S and E are backscatter and emissivity soil moisture sensitivities, respectively. The linear sensitivity assumption further allows the decomposition of the backscatter signal variance into $Var(\sigma_\theta^0) = S^2\sigma_\theta^2$, where σ_θ is the soil moisture standard deviation. The resulting bias factor is

$$B = \frac{S^2\sigma_\theta^2}{S^2\sigma_\theta^2 + \sigma_\eta^2} = \left(1 + \frac{\sigma_\eta^2}{S^2\sigma_\theta^2}\right)^{-1} \tag{8}$$

where σ_η is the backscatter error standard deviation. Combining (7) and (8) results in the following expression for β:

$$\beta = \frac{E}{S}\left(1 + \frac{\sigma_\eta^2}{S^2\sigma_\theta^2}\right)^{-1} \tag{9}$$

where the first factor denotes the error-free slope β_θ and the second factor accounts for biases due to measurement errors.

C. Coefficient of Determination R^2

The coefficient of determination of the relationship in (4) is given by

$$\begin{aligned} R^2 &= \frac{Cov\left(\sigma_\theta^0 + \eta, e_\theta + \nu\right)^2}{Var\left(\sigma_\theta^0 + \eta\right) Var\left(e_\theta + \nu\right)} \\ &= \frac{Cov\left(\sigma_\theta^0, e_\theta\right)^2}{\left(Var\left(\sigma_\theta^0\right) + \sigma_\eta^2\right)\left(Var\left(e_\theta\right) + \sigma_\nu^2\right)} \end{aligned} \tag{10}$$

which indicates the fraction of variance explained by the linear relationship and is equivalent to the squared correlation coefficient ρ^2 (we use the notation of R^2 throughout this study). σ_ν is the emissivity error standard deviation. The second equality follows from the error term assumptions. By decomposing the emissivity signal variance into $Var\left(e_\theta\right) = E^2\sigma_\theta^2$ (see equivalent backscatter decomposition in Section II-B), and using (7), it can be shown that

$$R^2 = \frac{E^2S^2\sigma_\theta^4}{\left(S^2\sigma_\theta^2 + \sigma_\eta^2\right)\left(E^2\sigma_\theta^2 + \sigma_\nu^2\right)} \tag{11}$$

where high soil moisture sensitivities and standard deviations are favorable to strong active–passive correlations, while measurement errors weaken the linear relationship. Note that R^2, in contrast to β, depends on both the radar and radiometer error terms, reflecting the symmetry of the correlation coefficient as opposed to the slope parameter.

TABLE I
SIMULATION SCENARIOS CONSIDERED IN THIS STUDY

Scenario	S & E	Kp	σ_ν^K	σ_θ
High Precision	TVM	0.07 (0.3 dB)	1.5 K	0.045 m^3m^{-3}
Low Precision	TVM	0.12 (0.5 dB)	2.5 K	0.045 m^3m^{-3}

D. Monte Carlo Simulations

Analytical formulations developed in Sections II-B and II-C rely on the assumption of linear backscatter and emissivity soil moisture sensitivities to ensure closed-form expressions. While this assumption is well-justified for simulations in this study (linear correlations exceeding 0.98 in all cases), possible approximation errors are quantified here. We conducted Monte Carlo simulations of all configurations considered in this study (adding random errors to numerical model outputs according to the two precision scenarios, not shown) and found median (maximum) differences with respect to analytical expressions of 0.001 (0.017) for R^2 and 0.01 (0.38) for β. Slope differences larger than 0.1 occurred only for magnitudes greater than 4. We conclude that the linear sensitivity assumption introduces marginal errors that are negligible for the purposes of this study.

E. Simulation Scenarios

The closed-form expressions in (9) and (11) are the basis for β and R^2 simulations conducted in this study. Table I lists the required parameters, which are derived as follows.

1) Soil Moisture Sensitivities: Backscatter and emissivity soil moisture sensitivities are derived from numerical simulations, further described in Section III. For each vegetation type, vegetation water content increment, and sensor configuration, the sensitivity estimation is conducted separately through linear regression along with a soil moisture range of 0.05–0.30 m^3m^{-3} (centered approximately on the mean of globally observed soil moisture states and capturing 83% of observed states based on SMAP data analysis, further described in Section IV).

2) Measurement Errors: We quantify radar errors through the Kp parameter and radiometer errors in units of Kelvin in accordance with conventions for instrument precision allocation [38]. Measurement noise depends on several factors such as instrument configuration, spatial resolution, and averaging. We consider two scenarios: the "High Precision" scenario assumes $Kp = 0.07$ (corresponding to 0.3 dB radar error allocation) and a radiometer uncertainty standard deviation of $\sigma_\nu^K = 1.5$ K. The superscript emphasizes the difference in units with respect to σ_ν. This scenario aims to provide a lower uncertainty bound for relationships between satellite radiometer and similar resolution scatterometer or aggregated SAR signatures, as investigated in several previous studies [9], [12], [20]. Note that these error estimates are conservative: Satellite scatterometers can show calibration errors (including noise-like and bias contributions) below 0.25 dB [39], and extensively aggregated SAR observations are considered to exhibit very low or negligible speckle noise [40]. Further, the SMAP radiometer uncertainty budget of 1.3 K is slightly lower than the estimate considered here [38]. However, since several other factors exist that can lead to noise-like signal disturbances, such as subpixel heterogeneity or azimuth angle effects [41], we consider the chosen error estimates reasonable lower uncertainty bounds for the purposes of this study. In the second scenario, named "Low Precision," we consider even more conservative error allocations of $Kp = 0.12$ (0.5 dB) and $\sigma_\nu^K = 2.5$ K, respectively. This scenario resembles a case where instrument noise or other signal disturbances are enhanced, for instance, due to a lower degree of SAR measurement aggregation. All calculations in (9) and (11) are carried out in linear units. The emissivity error term is converted using $\sigma_\nu = \sigma_\nu^K T^{-1}$ and assuming a physical temperature of $T = 288$ K. The backscatter error term is derived as described in the Appendix and assuming average soil moisture conditions centered on the soil moisture range used for sensitivity estimation.

3) Soil Moisture Variability: Soil moisture variability is a scale-dependent parameter influenced by several geophysical factors such as meteorological forcing, land use, and soil properties [42]–[45]. To provide an estimate for scales relevant to satellite observations, we analyzed SMAP soil moisture retrievals globally and found a median temporal soil moisture standard deviation of 0.044 m^3m^{-3} (for details of this analysis, including the filtering of nonvegetated areas and regions with negligible soil moisture variability, see Section IV). The spread in these estimates was reasonable with an interquartile range of 0.028–0.063 m^3m^{-3}. According to previous studies, these estimates can be considered conservative: Piles *et al.* [42] derived global soil moisture standard deviations based on multiyear satellite data time series and found a mode of approximately 0.045 m^3m^{-3}, a significantly higher median (not specified), and a considerable fraction of land areas exhibiting standard deviations larger than 0.10 m^3m^{-3}. Famiglietti *et al.* [43] analyzed data from thousands of *in situ* sensors and found a spatial standard deviation interquartile range of approximately 0.06–0.08 m^3m^{-3} for scales relevant to satellite observations. Based on the above considerations, and recognizing that soil moisture variability can vary considerably geographically, we consider the SMAP derived estimate (hereafter taken to be 0.045 m^3m^{-3}) reasonable for the purposes of this study.

III. Tor Vergata Model (TVM)

In this section, we describe the numerical model used for backscatter and emissivity simulations. We characterize the considered vegetation types and specify soil and sensor parameters. Finally, we summarize previous TVM validation studies.

A. Backscatter and Emissivity Simulations

The TVM is a discrete, radiative transfer-based microwave scattering and emission model for vegetated soils [31]. Simulations of active and passive signatures follow a consistent physical basis (for complete mathematical descriptions refer to [46]–[48]). The soil-vegetation medium is divided into three layers, indicated in Fig. 3. The rough surface soil is represented through the integral equation method [49]. Stems are modeled as vertically oriented cylinders. The upper canopy is modeled through sublayers of randomly distributed cylinders (representing branches, petioles, and needles) and disks (representing leaves). The scattering and extinction characteristics of the individual components are calculated using suitable electromagnetic approximations [50]–[53]. Soil, stem, and canopy contributions are combined by means of the matrix doubling algorithm [49], taking higher order scattering effects into account. The resulting bistatic scattering coefficient of the soil-vegetation medium is the basis for both backscatter and emissivity simulations. In the passive case, and assuming thermal equilibrium, the emissivity of the soil-vegetation medium is obtained from the bistatic scattering coefficient using Kirchhoff's law of energy conservation [54]. The brightness temperature Tb (measured by radiometer instruments) is related to the emissivity through

$$Tb = eT \tag{12}$$

where T denotes the effective physical temperature. In the active case, the backscatter coefficient σ^0 (measured by radar instruments) is obtained by evaluating the bistatic scattering coefficient in the backward direction [31]. The backscatter

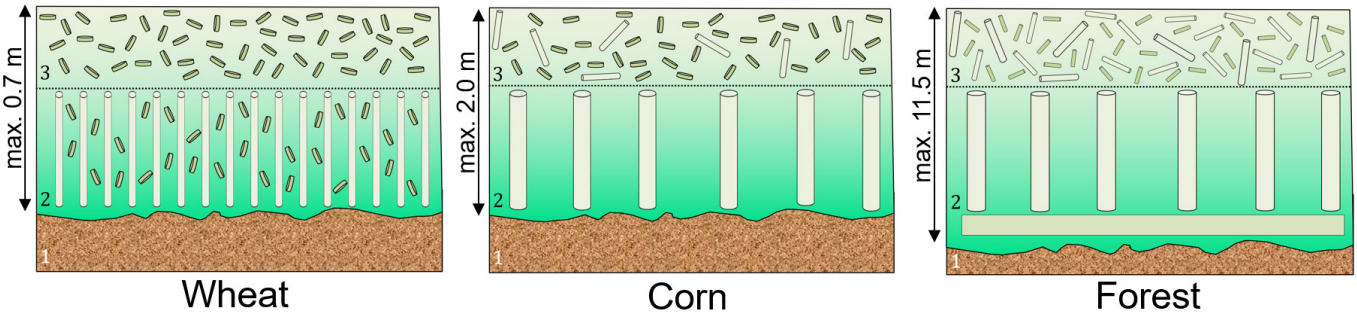

Fig. 3. Simplified schematic of the TVM geometry for corn, wheat, and coniferous forest. The three layers, soil (1), stems (2), and upper canopy (3), are indicated. Note different maximum heights for the three vegetation types.

coefficient can be decomposed into contributions from elementary scattering mechanisms as

$$\sigma^0 = \sigma^0_{\text{soil}} + \sigma^0_{\text{doub}} + \sigma^0_{\text{mult}} + \sigma^0_{\text{veg}} \tag{13}$$

where subscripts indicate contributions from soil surface scattering, double bounce, multiple soil-vegetation interactions, and vegetation volume scattering, respectively.

B. Wheat, Corn, and Forest Models

Three vegetation types are considered in this study: wheat, corn, and coniferous forest. These configurations are chosen since they differ significantly in geometry and have been extensively validated in previous experimental studies. Individual characteristics of model geometry (Fig. 3) and parameters (Table II) are summarized in the following. This includes the derivation of vegetation water content (VWC), which is defined as the total aboveground plant water per unit area and is not a direct input for the numerical model.

In the case of wheat, elliptical disks in the stem and upper canopy layers represent long-sheeted leaves. Stems are modeled as thin cylinders with an areal density of 600 m^{-2}. The full set of model parameters is based on *in situ* measurements acquired in [55], further described in [56]. Here, we model a wheat plant during its growing stage up to 70 cm, corresponding to a vegetation water content range of approximately 0–2.5 kg/m^2. Vegetation water content is derived directly from the *in situ* dataset. In the case of corn, small cylinders and disks in the upper canopy layer represent petioles and leaves, respectively. Stems are thicker than in the case of wheat and show a moderate areal density of 8 m^{-2}. The full parameter set is based on growth routines developed in previous experimental campaigns [57]. Here, we model the growing stage of a corn plant up to 200 cm, corresponding to a vegetation water content range of approximately 0–6.7 kg/m^2. Contrasting to [57], we assume constant plant moisture conditions to isolate the effects of growth, in accordance with findings in [58]. Vegetation water content is derived from the volumetric water fraction and volume of the individual plant components. Volumetric and gravimetric water fractions are related through an empirical relationship described in [59], assuming a dry matter density of 0.25 g/cm^3. In the case of forest, small and large cylinders in the upper canopy represent needles and branches, respectively. A purely attenuating understory layer is included that is parametrized with an optical depth of 0.2 Np [60]. The full parameter set is based on a dedicated field study [61] and allometric relations developed in [62]. Here, we model a coniferous forest stand with an increasing areal density of 0.05–0.1 m^{-2} (500–1000 trees per hectare), resulting in a dry biomass range of 60–130 tons per hectare and a vegetation water content range of approximately 7–14.5 kg/m^2. Tree height, stem diameter, and branch size are modeled as truncated distributions that are assumed to be constant. Vegetation water content is derived from the wet biomass and gravimetric moisture content of the individual plant components.

TABLE II

SELECTED TVM VEGETATION PARAMETERS. MOISTURE PERCENTAGES ARE GRAVIMETRIC

	Wheat	Corn	Forest
Nominal			
VWC	0-2.5 kg/m^2	0-6.7 kg/m^2	7-14.5 kg/m^2
Geometry			
Height	5-70 cm	10-200 cm	950* cm
Stem Density	600 m^{-2}	8 m^{-2}	0.05-0.1 m^{-2}
Stem Diameter	0.15-0.45 cm	0.5-3.5 cm	20* cm
Moisture			
Stems	~87 %	80 %	50 %
Branches/Petioles	–	80 %	60 %
Needles/Leaves	80 %	70 %	60 %

*Mean of truncated Gaussian distribution

C. Soil and Sensor Parameters

We consider two different frequency configurations, namely, L-band backscatter and L-band emissivity (L/L-band) and C-band backscatter and L-band emissivity (C/L-band). These configurations are analyzed for HH/H and VV/V active/passive polarizations (hereafter referred to as "H-polarization" and "V-polarization," respectively), an incidence angle of 40°, a radiometer frequency of 1.4 GHz (L-band), and radar frequencies of 1.26 GHz (L-band) and 5.4 GHz (C-band). Incidence angle effects are not investigated. Concerning soil parameters, we consider a surface roughness root mean square height of 1.0 cm and the autocorrelation length of 5.0 cm with an exponential autocorrelation function. These parameters correspond to typical roughness conditions in natural settings and have been tested against experimental data in

TABLE III

PREVIOUS TVM VALIDATION STUDIES FOR THE CONSIDERED VEGETATION AND SENSOR CONFIGURATIONS. ENTRIES MARKED WITH "*" INDICATE DECIDUOUS FOREST STUDIES. ROOT MEAN SQUARE (RMS) ERRORS ARE PROVIDED IF AVAILABLE, LISTED IN THE SAME ORDER AS THE CORRESPONDING REFERENCES. UNITS CORRESPOND TO DECIBEL (DB), EMISSIVITY (–), AND KELVIN (K)

Vegetation Type	Sensor Type	Frequency	RMS Error	Reference
Wheat	Active	C-band (5.3 GHz)	1.78-2.23 (dB), 2.0 (dB)	[57], [63]
	Active	L-band (1.3 GHz)	1.5-3.0 (dB)	[64]
	Passive	L-band (1.4 GHz)	0.03 (-), 6.44-9.15 (K)	[56], [65]
Corn	Active	C-band ($4.6 - 5.4$ GHz)	0.96-1.44 (dB), –, 1.57 (dB)	[57], [66], [67]
	Active	L-band ($1.2 - 2.5$ GHz)	–, 1.39 (dB)	[66], [67]
	Passive	L-band (1.4 GHz)	4.14-9.83 (K)	[65]
Forest	Active	C-band (5.3 GHz)	1.01 (dB)	[68]
	Active	L-band (1.2 GHz)	– , 0.95 (dB), –	[48], [69]*, [66]
	Passive	L-band (1.4 GHz)	–, 2.56 (K), 0.0076 (-), –	[47]*, [70], [71]*, [59]

previous studies [31], [56], [57]. The conversion between permittivity and soil moisture content is conducted using the dielectric model of [72], assuming a nominal clay fraction of 15%.

D. Validation With Experimental Data

Table III provides an overview of previous TVM validation studies for each vegetation type and sensor configuration considered here. Root mean square (RMS) errors between observations and simulations are listed where possible. Since the basic models are similar [47], [48], both coniferous and deciduous forest studies are included. In summary, RMS errors are in the range of 0.95–3.0 dB for active simulations and 2.56–9.83 K and 0.0076–0.03 emissivity units for passive simulations. Notice that errors exceeding 4 K, reported in [65], are for large dynamic ranges on the order of 25–80 K and with respect to ground-based observations of limited absolute accuracy (3 K for the wheat case). Given that experimental data sets suffer from their own error sources such as instrument noise, the reported model-observation agreements can be considered reasonable. Overall, the presented validation record provides a satisfactory basis for conducting simulations across several vegetation types and frequencies in this study.

IV. SATELLITE DATA

All satellite data analysis in this study is conducted in the period of April 13 to July 7, 2015, consistent with SMAP radar data availability. To estimate global soil moisture statistics in Section II-E, we use SMAP radiometer soil moisture retrievals [73]. Only recommended quality retrievals are included based on the provided flags. For consistency with our simulations we mask nonvegetated areas based on International Geosphere-Biosphere Programme (IGBP) classification and regions of negligible soil moisture variability during the study period ($\sigma_\theta < 0.01$ m^{3}m^{-3}). This excludes roughly 13.5% and 2.5% of global land area, respectively, affecting mostly desert regions that are not relevant to the analysis conducted here. To assess global active–passive relationships in Section V-D, we analyze observations from SMAP and the Advanced Scatterometer (ASCAT) instrument onboard the EUMETSAT MetOp satellites [74]. For SMAP, we use L-band V-polarized Tb observations that are posted on a 36-km global EASE-grid [73]. The data are converted to emissivity using ancillary effective land surface temperature information that is used for SMAP science products and provided within the SMAP project public-distribution data files. We also use SMAP L-band VV-polarized backscatter observations [75], which we aggregate to the radiometer grid-scale excluding the nadir region in a 90-km range. For ASCAT, we use C-band VV-polarized backscatter observations normalized to 40° incidence angle, obtained from the H115 soil moisture climate data record [76]. We re-grid the data to match with SMAP through nearest neighbor resampling, using both MetOp-A and MetOp-B observations to maximize temporal overlap. We filter all data for radio frequency interference, mountainous terrain, frozen or snow-covered regions, and proximity to water bodies, using SMAP ancillary data. Nonvegetated areas and regions of negligible soil moisture variability are also excluded (see methodology described above). The resulting active and passive data pairs are used to estimate β and R^2 globally through linear regression, requiring a minimum of ten paired observations and excluding regions with nonnegative slopes. Global time-averaged vegetation water content estimates are derived from SMAP ancillary data [77] based on a Normalized Difference Vegetation Index (NDVI) climatology observed by the MODIS instrument.

V. RESULTS AND DISCUSSION

A. Slope β

Fig. 4 shows simulation results of the active-passive slope β. The slope quantifies the coupling strength between backscatter and emissivity signatures, with higher magnitudes (larger negative values) indicating stronger coupling. Results are discussed with reference to radar and radiometer soil moisture sensitivities (Fig. 6) where applicable. Our discussion focusses on the two precision scenarios, hereafter referred to as "slope" or "β." The error-free slope β_θ is considered purely as a theoretical upper bound.

Both the L/L-band and C/L-band configurations show nonzero slopes. This suggests that coupling between backscatter and emissivity signatures can be established across frequencies and over a range of vegetation conditions. Nonzero slopes (defined here as magnitudes larger than 0.5) occur up to 6.3 kg/m^2 in L/L-band and 2 kg/m^2 in C/L-band, assuming V-polarization and the "High Precision" scenario. In H-polarization, slope magnitudes are retained for slightly

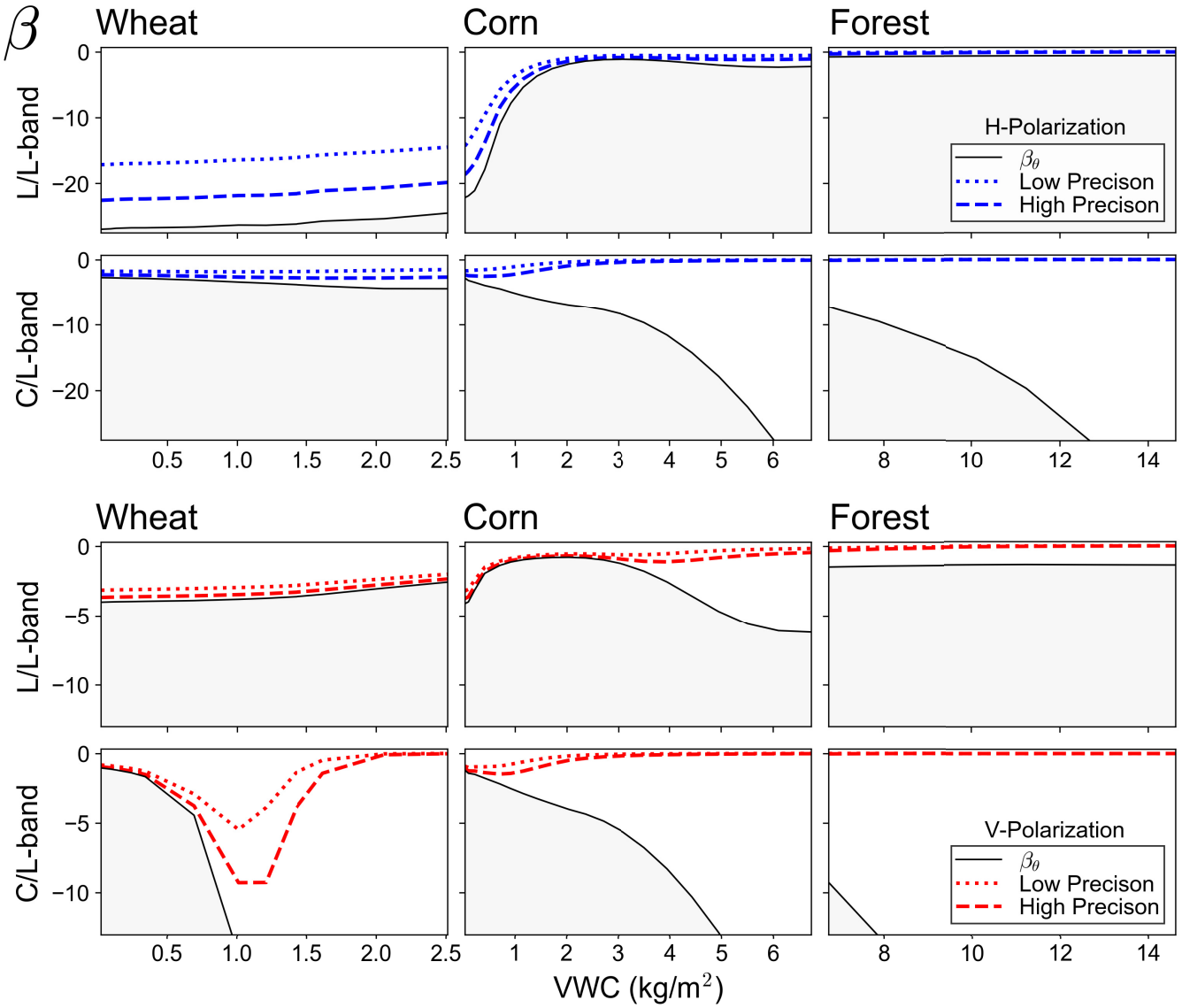

Fig. 4. Slope β $(-)$ between backscatter and emissivity, simulated after (9). Results are displayed for H-polarization (upper two rows) and V-polarization (lower two rows). Axis limits are adjusted to fit the dynamic ranges of the respective polarizations and vegetation types. Low and high measurement precision scenarios and error-free conditions (β_θ) are indicated. The area below β_θ is shaded gray since it presents an upper bound for the magnitude of β.

higher vegetation water contents. For the "Low Precision" scenario, generally lower magnitudes arise.

Slope magnitudes show an overall decreasing trend with increasing vegetation water content. This is consistent with findings of previous studies [20], [32], [36] and suggests that the active–passive coupling strength decreases with increasing vegetation cover. According to (9), the trend can be explained by decreasing radar and radiometer soil moisture sensitivities. Three mechanisms can be differentiated: First, for decreasing radar sensitivities, slope magnitudes decrease due to increasing bias effects (visible as large differences between β_θ and β). Second, for decreasing radiometer sensitivities and constant or increasing radar sensitivities, slope magnitudes decrease since β_θ is shifted toward zero (visible, e.g., for corn in L/L-band). Third, for decreasing radar and radiometer sensitivities, both above-named effects can occur jointly (visible, e.g., in the case of forest in L/L-band).

The first mechanism, that is, the occurrence of bias effects, is particularly noteworthy since it is not accounted for in previous simulation studies [31], [32]. Specifically, significant biases are evident for configurations that show low radar soil moisture sensitivities (mostly occurring in C/L-band given moderate or high vegetation cover conditions). This suggests that the coupling strength that is observable by satellite instruments (denoted by β) can be significantly lower than the underlying linear relationship (denoted by β_θ) when the backscatter soil moisture signal becomes small with respect to the measurement uncertainty. Note that β, as opposed to β_θ, represents the "optimal" (in a least-squares

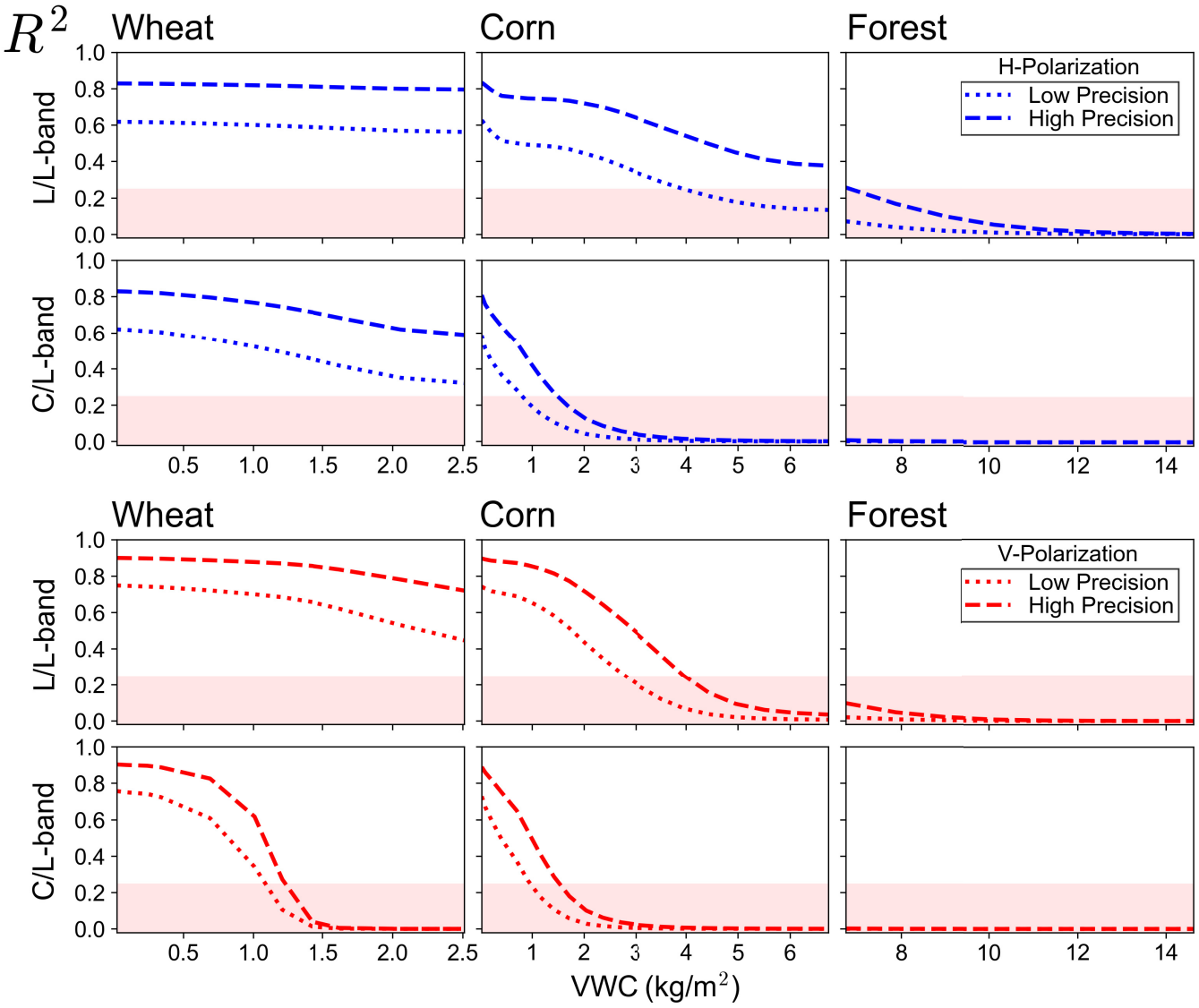

Fig. 5. Coefficient of determination R^2 $(-)$ of the linear relationship between backscatter and emissivity, simulated after (11). Red shading indicates a threshold of $R^2 > 0.25$. Figure panels are the same as in Fig. 4.

sense) slope parameter for estimating emissivity signatures in a given precision scenario. While a variety of measurement error levels can occur in practical applications, errors as low as $Kp < 0.01$ would lead to substantial biases (not shown) as backscatter sensitivities converge to zero for certain configurations (Fig. 6). Consequently, and since satellite data may include noise-like signal disturbances due to azimuth angle effects or subpixel heterogeneity, slope parameter biases may apply even when backscatter observations are extensively averaged. Slope biases may also occur as a result of negligible soil moisture variability (not investigated). Potential implications for algorithm parameter estimation in the context of SMAP are beyond the scope of this study but deserve attention in future research. For interpretation of the above descriptions, note that bias magnitudes effectively scale with the dB-unit backscatter sensitivity S^{dB} (instead of its linear unit counterpart S) since the Kp error model leads to a constant backscatter error allocation in dB units.

Dynamics of β vary between different vegetation types. This indicates a dependence on plant structure and geometry in addition to the aforementioned more general dependence on vegetation cover, consistent with findings of previous studies [32]. The main distinctions are listed in the following. Wheat simulations show low slope dynamics in most cases, explained by well-retained soil moisture sensitivities for the full vegetation water content range. As the only exception, wheat simulations in C/L-band and V-polarization show nonmonotonic slope dynamics. This is explained by a sharp decrease of C-band radar sensitivities, leading to a sharp increase in β_θ magnitudes that causes β magnitudes to temporarily increase until noise effects become dominant. While we expect generally stronger vegetation attenuation at higher frequencies [78], this behavior is likely attributed to an overestimation of

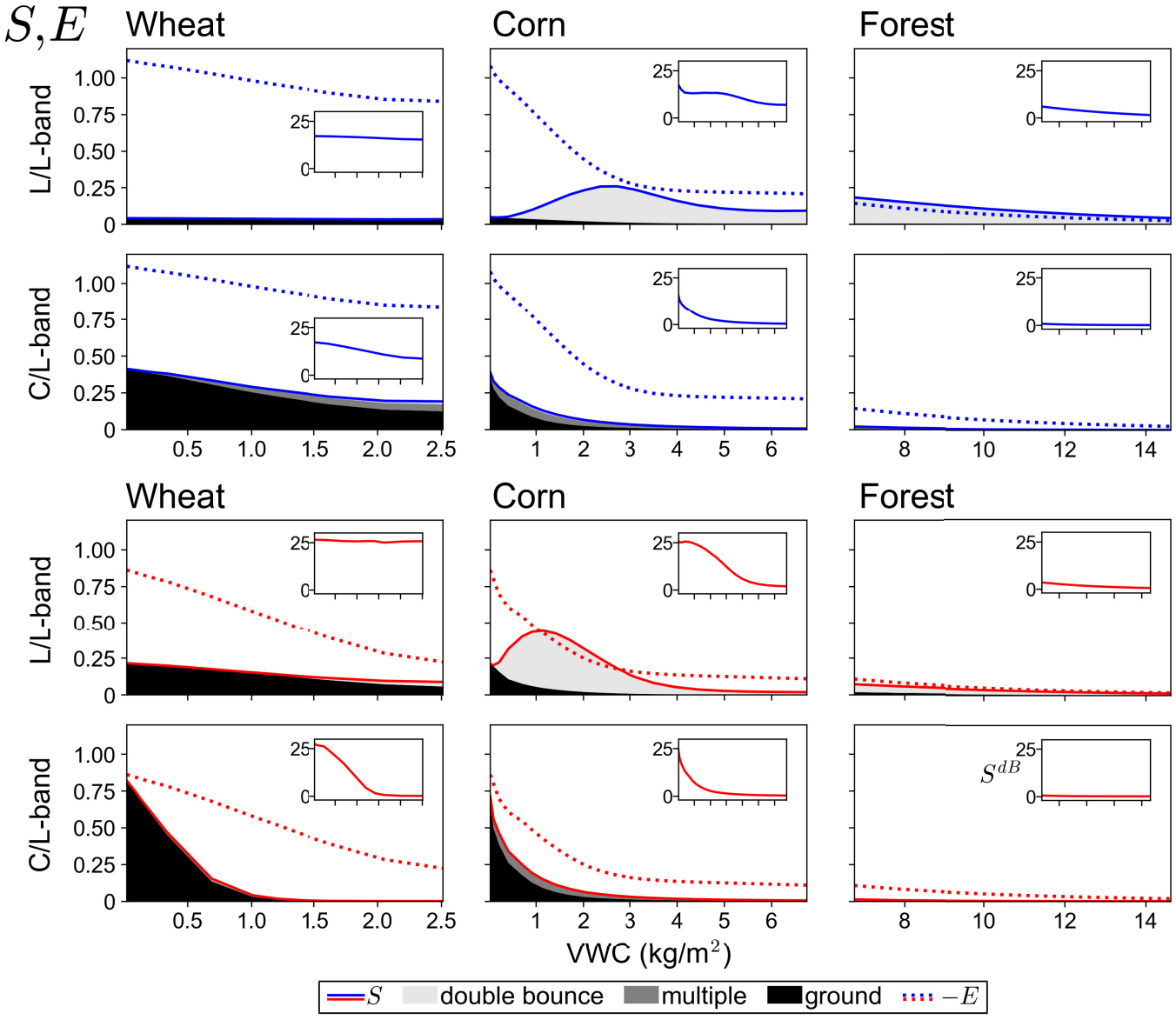

Fig. 6. Simulated backscatter sensitivity to soil moisture S $(-/\mathrm{m}^3\mathrm{m}^{-3})$ and emissivity sensitivity to soil moisture E $(-/\mathrm{m}^3\mathrm{m}^{-3})$. Contributions of double bounce, multiple scattering, and surface scattering are indicated. Insets show the dB-unit backscatter sensitivity to soil moisture S^{dB} $(\mathrm{dB}/\mathrm{m}^3\mathrm{m}^{-3})$, using the same x-axis ranges and ticks. Note that E is identical for both frequency configurations. Figure panels are the same as in Figs. 4 and 5.

C-band V-polarized signal attenuation from the dense vertical wheat stems, further discussed in Section V-C. By the same explanation, the sharp increase of β_θ magnitudes likely causes an overestimation of the effect of different noise levels, that is, β magnitude differences between the two precision scenarios (larger than 5 at the inflection point) significantly exceed typical differences (median of 0.4 for all other configurations). For corn, we find significant slope dynamics in all configurations, which is explained by decreasing radar sensitivities due to attenuation effects (C/L-band) and temporarily increasing radar sensitivities due to double bounce (L/L-band). Note that corn simulations, in contrast to wheat, exhibit generally monotonic slope dynamics since C-band radar sensitivities do not show a disproportionally sharp or polarization-dependent decrease. For forest, we find overall low slope magnitudes and dynamics due to bias effects (C/L-band) or low radar and radiometer soil moisture sensitivities (L/L-band).

B. Coefficient of Determination R^2

Fig. 5 shows simulation results of the coefficient of determination R^2, which quantifies the strength of the linear relationship between active and passive signals. Only the two precision scenarios are displayed since we find approximately unity (larger than 0.99) correlations for the error-free case. Results are discussed with reference to radar and radiometer soil moisture sensitivities (Fig. 6) where applicable.

Both the L/L-band and C/L-band configurations show considerable active–passive correlations. This suggests that a linear relationship between backscatter and emissivity, as embedded in the SMAP downscaling algorithm, can hold across frequencies and over a range of vegetation conditions. Moderate or higher correlations (defined as $R^2 > 0.25$ in this study, noting that synergies can retain meaningful information below this threshold) are retained up to 4 kg/m^2 in L/L-band and 1.5 kg/m^2 in C/L-band, assuming V-polarization and the "High Precision" scenario. Note that both frequency configurations show comparable R^2 magnitudes for low vegetation water contents, suggesting that the strength of the linear relationship across frequencies (C-band backscatter and L-band emissivity) can be comparable to the original SMAP configuration (L-band backscatter and L-band emissivity) for low vegetation cover conditions. Note also that the vegetation cover thresholds are sensitive to vegetation type, precision scenario, and polarization: for example, generally lower thresholds arise for the "Low Precision" scenario, while higher thresholds are obtained in H-polarization. Finally, note that vegetation water content thresholds for R^2 are lower with respect to thresholds reported for β. This highlights the complementarity of both metrics with respect to potential downscaling applications: while low correlations may indicate increasing accuracy limitations, nonzero slopes can imply that active–passive synergies still contain useful information.

Magnitudes of R^2 decrease with increasing vegetation water content. This finding is in agreement with previous studies [15], [20] and reflects decreasing radar and radiometer soil moisture sensitivities. Radar sensitivities act as the main limiting factor, such that R^2 dynamics in Fig. 5 are in close agreement with S^{dB} dynamics in Fig. 6 (notice that, equivalent to aforementioned β biases, R^2 dynamics scale with the dB-unit backscatter sensitivity S^{dB}). Note also that C/L-band V-polarized simulations of wheat might underestimate R^2 magnitudes due to an overestimation of signal attenuation, further discussed in Section V-C.

C. Radar and Radiometer Sensitivities to Soil Moisture

Fig. 6 shows simulated backscatter and emissivity soil moisture sensitivities. Contributions from double bounce, multiple scattering, and surface scattering are indicated. Emissivity and surface scattering sensitivities are indicative of one- and two-way vegetation attenuation, respectively. Insets show the dB-unit backscatter sensitivity S^{dB}.

Increasing vegetation cover generally leads to decreasing soil moisture sensitivities. This trend is in agreement with previous studies [24], [79] and is explained by increasing signal attenuation from plant constituents. Note that linear unit backscatter sensitivities can temporarily increase when strong double bounce effects occur, such as for corn in L-band. Contrarily, backscatter sensitivities in dB units show generally monotonic decreasing trends. Similar results are reported in [80].

We describe vegetation-type-specific trends in the following, discussing model geometry (Fig. 3) where applicable. In the case of wheat, soil moisture sensitivities are generally well retained over the vegetation water content range. As the only exception, C-band VV-polarized backscatter shows a strong sensitivity decrease. This effect is attributed to vertical stem attenuation, as suggested by its polarization dependence and findings in previous studies [56], [57]. A potential overestimation of stem attenuation is discussed later in this section. Interactions with the canopy are generally low at L-band such that soil scattering is dominant. Considerable multiple scattering is observed for C-band HH-polarized radar signatures, suggesting interactions with leaves in the canopy. In the case of corn, emissivity sensitivities show a strong initial decrease (suggesting increasing stem and canopy attenuation) but retain considerable magnitudes even for high vegetation water contents. Emissivity sensitivities are consistently higher in H-polarization with respect to V-polarization, suggesting polarization-dependent attenuation from the vertically oriented stems. For L-band backscatter sensitivities, double bounce effects are dominant in both polarizations. VV-polarized double bounce effects peak and decline for lower vegetation water contents with respect to HH-polarization, suggesting again polarization-dependent signal interactions with the vertical stems. For C-band backscatter sensitivities, strong attenuation and multiple scattering effects are evident in both polarizations, the latter mechanism suggesting interactions with the randomly distributed upper canopy constituents. In the case of forest, backscatter and emissivity sensitivities are generally low, with C-band backscatter showing almost no sensitivity. This is in agreement with the expectation of substantial canopy attenuation, which has been attributed mainly to branch interactions in previous studies [59], [60]. Note, however, that L-band HH-polarized backscatter retains considerable sensitivity due to double bounce effects.

Recent studies suggest that radiative transfer modeling of long vertical stems can lead to an overestimation of vegetation attenuation [81], [82], particularly for high areal stem densities. This potentially explains the strong simulated sensitivity decrease in C-band VV-polarized radar signatures over wheat, leading to anomalous slope dynamics in this case (Figs. 4 and 7). Despite comparisons with satellite observations show reasonable agreements in all other cases (Fig. 7), simulations in this study could underestimate soil moisture sensitivities for configurations where unaccounted transmission or coherent scattering effects (e.g., due to large canopy gaps or inhomogeneous scatterer distributions) are important. While this would translate into more conservative rather than overestimated β and R^2 magnitudes, comparisons of our results with full-wave simulations are desirable targets for future studies.

D. Comparison With Global Satellite Retrievals

Fig. 7 compares β and R^2 simulations to global statistical retrievals from SMAP and ASCAT data. Simulations correspond to the "High Precision" scenario (Section II-E).

Simulations and satellite retrievals show comparable β magnitudes that exhibit similar trends with increasing vegetation cover. As the only exception, wheat simulations in C/L-band overestimate slope magnitudes for vegetation water contents

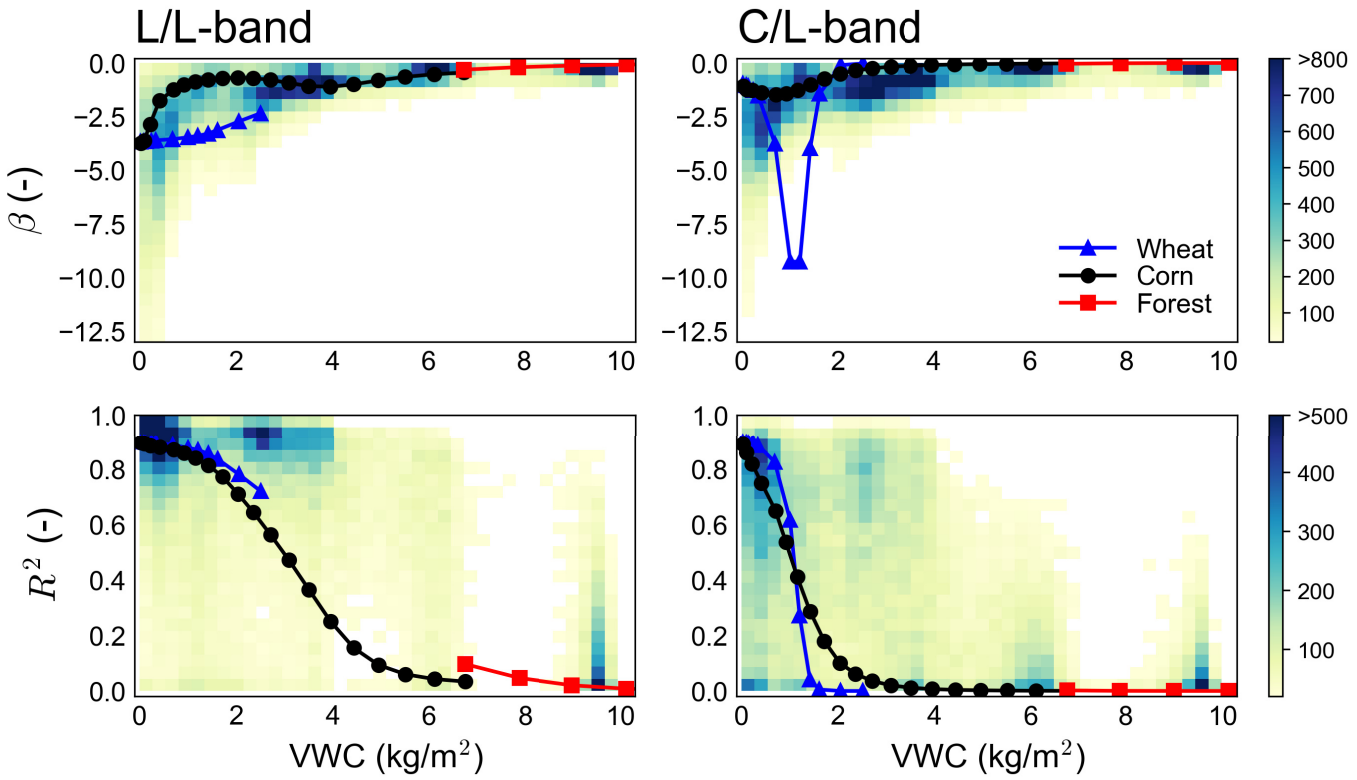

Fig. 7. Comparison of β and R^2 simulations (lines) with satellite retrievals (density plots). Satellite data correspond to SMAP (L/L-band) and ASCAT/SMAP (C/L-band) active and passive microwave observations. Simulations correspond to the "High Precision" scenario. All results are in V-polarization. The minimum displayed density count is 20. Slope simulations for wheat in C/L-band are discussed in the text.

around 1 kg/m^2. This is likely explained by an overestimation of vegetation attenuation as discussed in Section V-C. For R^2, while simulations reasonably capture the main retrieval density hotspots and trends, unresolved retrievals remain particularly for intermediate vegetation cover conditions. R^2 retrievals also show significantly larger spreads with respect to β. This indicates an enhanced sensitivity to confounding factors in addition to vegetation cover, consistent with findings of previous studies [29], [36]. Specifically, unresolved retrievals around 2–3 kg/m^2 are partly attributed to regions with enhanced soil moisture variability (e.g., Sudano-Sahel, not shown), explaining that simulations (based on median global soil moisture variability conditions) underestimate R^2 magnitudes in these cases. A potential overestimation of vegetation attenuation for wheat in C/L-band may be another contributing factor. Note that comparisons between our simulations and satellite retrievals inherently include a number of potential sources of mismatch, including unresolved vegetation structural or soil roughness conditions, subpixel heterogeneity, time-varying land cover conditions, or global vegetation water content estimates, based on optical data. Overall, while satellite observations encompass a wide range of land cover conditions that cannot be fully resolved by a limited number of model configurations, the vegetation-type-specific simulations conducted in this study reasonably capture magnitudes and major trends found across global satellite-scale retrievals.

VI. Conclusion

In this study, we investigate the relationship between active and passive microwave signatures that capture surface soil moisture changes under a vegetation canopy. We conduct numerical simulations and analyze global satellite data to find that a linear relationship—with slope β and coefficient of determination R^2—between backscatter and emissivity can be established over a range of vegetation conditions. We quantify the range and extent of the relationship as a function of the vegetation water content.

The coupling between active and passive signals decreases with increasing vegetation water content. Moderate or higher correlations (nonzero slopes) are simulated up to 4 kg/m^2 (6.3 kg/m^2) for L-band backscatter and L-band emissivity and 1.5 kg/m^2 (2 kg/m^2) for C-band backscatter and L-band emissivity. While these thresholds depend on polarization and measurement error assumptions, our results suggest that linear active–passive relationships can be established within vegetation cover ranges relevant to the SMAP and Sentinel-1/SMAP combined soil moisture products [9], [12]. Active–passive relationships also depend on the vegetation type, which is explained by different scattering and attenuation mechanisms affecting radar and radiometer responses. The simulations capture magnitudes and trends found across global satellite-scale retrievals; however, simulations track retrievals only if measurement errors are taken into account.

Analytical formulations, developed in this study, suggest that the active–passive slope is biased (and the linear relationship is weakened) when radar (radar and radiometer) measurements are subject to noise. Slope biases increase as the radar soil moisture sensitivity decreases, particularly affecting the C-band radar and L-band radiometer configuration for moderate to high vegetation cover conditions. While such effects are not accounted for in previous simulation studies [31], [32], potential implications for algorithm parameter estimation in the context of SMAP deserve attention in future research.

This study investigates the first foundation of the SMAP downscaling approach, that is, the covariation of active and passive microwave signatures. The second foundation, that is, the combination of multiresolution data, includes additional aspects (e.g., subpixel heterogeneity) that require dedicated investigations in future studies. Further studies may also assess coherent scattering and canopy gap transmission effects, not accounted for in the radiative transfer scheme adopted here, and different soil roughness and soil moisture variability conditions, not investigated here. Overall, this study provides new insights into the coupling of active and passive microwave signals over land, aimed at assisting synergies between current and future satellite sensors across frequencies.

APPENDIX

We consider the backscatter terms σ^0 and σ^0_θ from (2). A standard error model for multiplicative noise is given by

$$\sigma^0 = \sigma^0_\theta(1 + Kp\omega) = \sigma^0_\theta + \sigma^0_\theta \; Kp\omega$$

where $\omega \sim N(0,1)$ and Kp is a dimensionless term scaling the backscatter noise standard deviation. Following the notation of (2) we define $\eta = \sigma^0_\theta Kp\omega$, noting that $Cov(\eta, \sigma^0_\theta) = 0$. The expectation and variance of η are given by

$$E[\eta] = E\left[\sigma^0_\theta \; Kp\omega\right] = KpE\left[\sigma^0_\theta\right] E\left[\omega\right] = 0$$

$$\sigma^2_\eta = Var\left(\sigma^0_\theta \; Kp\omega\right) = Kp^2 \; E\left[\left(\sigma^0_\theta\right)^2\right]$$

with $E[.]$ denoting the expected value and the last equality following

$$\begin{aligned} &Var\left(\sigma^0_\theta \; Kp\omega\right) = Kp^2 Var(\sigma^0_\theta\omega) \\ &= Kp^2\left\{Cov\left[\left(\sigma^0_\theta\right)^2, \omega^2\right] + E\left[\left(\sigma^0_\theta\right)^2\right] E\left[\omega^2\right] - E\left[\sigma^0_\theta\omega\right]^2\right\} \\ &= Kp^2 \; E\left[\left(\sigma^0_\theta\right)^2\right] \end{aligned}$$

since

$$Cov\left[\left(\sigma^0_\theta\right)^2, \omega^2\right] = 0$$

$$E\left[\omega^2\right] = 1$$

$$E\left[\sigma^0_\theta\omega\right] = 0.$$

ACKNOWLEDGMENT

The authors gratefully acknowledge support from the MIT-Germany Seed Fund "Global Water Cycle and Environmental Monitoring Using Active and Passive Satellite-Based Microwave Instruments." They also thank three anonymous reviewers for their comments on a previous draft of this work.

REFERENCES

[1] D. Entekhabi *et al.*, "The soil moisture active passive (SMAP) mission," *Proc. IEEE*, vol. 98, no. 5, pp. 704–716, May 2010.

[2] Y. H. Kerr *et al.*, "The SMOS mission: New tool for monitoring key elements ofthe global water cycle," *Proc. IEEE*, vol. 98, no. 5, pp. 666–687, May 2010.

[3] I. E. Mladenova *et al.*, "Remote monitoring of soil moisture using passive microwave-based techniques—Theoretical basis and overview of selected algorithms for AMSR-E," *Remote Sens. Environ.*, vol. 144, pp. 197–213, Mar. 2014.

[4] W. Wagner *et al.*, "The ASCAT soil moisture product: A review of its specifications, validation results, and emerging applications," *Meteorologische Zeitschrift*, vol. 22, no. 1, pp. 5–33, Feb. 2013.

[5] S. I. Seneviratne, "Investigating soil moisture–climate interactions in a changing climate: A review," *Earth-Sci. Rev.*, vol. 99, no. 3, pp. 125–161, May 2010.

[6] P. de Rosnay, M. Drusch, D. Vasiljevic, G. Balsamo, C. Albergel, and L. Isaksen, "A simplified extended Kalman filter for the global operational soil moisture analysis at ECMWF," *Quart. J. Roy. Meteorological Soc.*, vol. 139, no. 674, pp. 1199–1213, Jul. 2013.

[7] N. Wanders, D. Karssenberg, A. de Roo, S. M. de Jong, and M. F. P. Bierkens, "The suitability of remotely sensed soil moisture for improving operational flood forecasting," *Hydrol. Earth Syst. Sci.*, vol. 18, no. 6, pp. 2343–2357, Jun. 2014.

[8] J. D. Bolten, W. T. Crow, X. Zhan, T. J. Jackson, and C. A. Reynolds, "Evaluating the utility of remotely sensed soil moisture retrievals for operational agricultural drought monitoring," *IEEE J. Sel. Topics Appl. Earth Observ. Remote Sens.*, vol. 3, no. 1, pp. 57–66, Mar. 2010.

[9] N. N. Das *et al.*, "The SMAP mission combined active-passive soil moisture product at 9 km and 3 km spatial resolutions," *Remote Sens. Environ.*, vol. 211, pp. 204–217, Jun. 2018.

[10] J. Peng, A. Loew, O. Merlin, and N. E. C. Verhoest, "A review of spatial downscaling of satellite remotely sensed soil moisture," *Rev. Geophys.*, vol. 55, no. 2, pp. 341–366, Jun. 2017.

[11] S. Sabaghy *et al.*, "Comprehensive analysis of alternative downscaled soil moisture products," *Remote Sens. Environ.*, vol. 239, Mar. 2020, Art. no. 111586.

[12] N. N. Das *et al.*, "The SMAP and copernicus Sentinel 1A/B microwave active-passive high resolution surface soil moisture product," *Remote Sens. Environ.*, vol. 233, Nov. 2019, Art. no. 111380.

[13] T. Jagdhuber *et al.*, "Estimation of active-passive microwave covariation using SMAP and Sentinel-1 data," *Remote Sens. Environ.*, vol. 225, pp. 458–468, May 2019.

[14] N. N. Das, D. Entekhabi, R. S. Dunbar, E. G. Njoku, and S. H. Yueh, "Uncertainty estimates in the SMAP combined active–passive downscaled brightness temperature," *IEEE Trans. Geosci. Remote Sens.*, vol. 54, no. 2, pp. 640–650, Feb. 2016.

[15] N. N. Das, D. Entekhabi, and E. G. Njoku, "An algorithm for merging SMAP radiometer and radar data for high-resolution soil-moisture retrieval," *IEEE Trans. Geosci. Remote Sens.*, vol. 49, no. 5, pp. 1504–1512, May 2011.

[16] X. Wu, J. P. Walker, C. Rudiger, and R. Panciera, "Effect of land-cover type on the SMAP active/passive soil moisture downscaling algorithm performance," *IEEE Geosci. Remote Sens. Lett.*, vol. 12, no. 4, pp. 846–850, Apr. 2015.

[17] X. Wu, J. P. Walker, N. N. Das, R. Panciera, and C. Rüdiger, "Evaluation of the SMAP brightness temperature downscaling algorithm using active–passive microwave observations," *Remote Sens. Environ.*, vol. 155, pp. 210–221, Dec. 2014.

[18] C. Montzka *et al.*, "Investigation of SMAP fusion algorithms with airborne active and passive L-band microwave remote sensing," *IEEE Trans. Geosci. Remote Sens.*, vol. 54, no. 7, pp. 3878–3889, Jul. 2016.

[19] D. J. Leroux *et al.*, "Active–passive soil moisture retrievals during the SMAP validation experiment 2012," *IEEE Geosci. Remote Sens. Lett.*, vol. 13, no. 4, pp. 475–479, Apr. 2016.

[20] M. Piles, K. A. McColl, D. Entekhabi, N. Das, and M. Pablos, "Sensitivity of aquarius active and passive measurements temporal covariability to land surface characteristics," *IEEE Trans. Geosci. Remote Sens.*, vol. 53, no. 8, pp. 4700–4711, Aug. 2015.

[21] P.-W. Liu, J. Judge, R. D. De Roo, A. W. England, and T. Bongiovanni, "Uncertainty in soil moisture retrievals using the SMAP combined active–passive algorithm for growing sweet corn," *IEEE J. Sel. Topics Appl. Earth Observ. Remote Sens.*, vol. 9, no. 7, pp. 3326–3339, Jul. 2016.

[22] R. Panciera *et al.*, "The soil moisture active passive experiments (SMAPEx): Toward soil moisture retrieval from the SMAP mission," *IEEE Trans. Geosci. Remote Sens.*, vol. 52, no. 1, pp. 490–507, Jan. 2014.

[23] E. G. Njoku *et al.*, "Observations of soil moisture using a passive and active low-frequency microwave airborne sensor during SGP99," *IEEE Trans. Geosci. Remote Sens.*, vol. 40, no. 12, pp. 2659–2673, Dec. 2002.

[24] U. Narayan, "Retrieval of soil moisture from passive and active L/S band sensor (PALS) observations during the soil moisture experiment in 2002 (SMEX02)," *Remote Sens. Environ.*, vol. 92, no. 4, pp. 483–496, Sep. 2004.

[25] U. Narayan, V. Lakshmi, and T. J. Jackson, "High-resolution change estimation of soil moisture using L-band radiometer and radar observations made during the SMEX02 experiments," *IEEE Trans. Geosci. Remote Sens.*, vol. 44, no. 6, pp. 1545–1554, Jun. 2006.

[26] R. Bindlish and A. P. Barros, "Subpixel variability of remotely sensed soil moisture: An inter-comparison study of SAR and ESTAR," *IEEE Trans. Geosci. Remote Sens.*, vol. 40, no. 2, pp. 326–337, Aug. 2002.

[27] C. Rudiger, C.-H. Su, D. Ryu, and W. Wagner, "Disaggregation of low-resolution L-band radiometry using C-band radar data," *IEEE Geosci. Remote Sens. Lett.*, vol. 13, no. 10, pp. 1425–1429, Oct. 2016.

[28] C. Rudiger, M. Doubkova, J. R. Larsen, W. Wagner, and J. P. Walker, "Similarities between spaceborne active and airborne passive microwave observations at 1 km resolution," *IEEE Geosci. Remote Sens. Lett.*, vol. 11, no. 12, pp. 2178–2182, Dec. 2014.

[29] L. He, Y. Hong, X. Wu, N. Ye, J. P. Walker, and X. Chen, "Investigation of SMAP active–passive downscaling algorithms using combined Sentinel-1 SAR and SMAP radiometer data," *IEEE Trans. Geosci. Remote Sens.*, vol. 56, no. 8, pp. 4906–4918, Aug. 2018.

[30] E. Ghafari *et al.*, "On the impact of C-band in place of L-band radar for SMAP downscaling," *Remote Sens. Environ.*, vol. 251, Dec. 2020, Art. no. 112111.

[31] L. Guerriero, P. Ferrazzoli, C. Vittucci, R. Rahmoune, M. Aurizzi, and A. Mattioni, "L-band passive and active signatures of vegetated soil: Simulations with a unified model," *IEEE J. Sel. Topics Appl. Earth Observ. Remote Sens.*, vol. 9, no. 6, pp. 2520–2531, Jun. 2016.

[32] T. Jagdhuber *et al.*, "Physics-based modeling of active and passive microwave covariations over vegetated surfaces," *IEEE Trans. Geosci. Remote Sens.*, vol. 57, no. 2, pp. 788–802, Feb. 2019.

[33] K. A. McColl *et al.*, "Global characterization of surface soil moisture drydowns," *Geophys. Res. Lett.*, vol. 44, no. 8, pp. 3682–3690, Apr. 2017.

[34] A. G. Konings, M. Piles, K. Rötzer, K. A. McColl, S. K. Chan, and D. Entekhabi, "Vegetation optical depth and scattering albedo retrieval using time series of dual-polarized L-band radiometer observations," *Remote Sens. Environ.*, vol. 172, pp. 178–189, Jan. 2016.

[35] K. A. McColl, S. H. Alemohammad, R. Akbar, A. G. Konings, S. Yueh, and D. Entekhabi, "The global distribution and dynamics of surface soil moisture," *Nature Geosci.*, vol. 10, no. 2, p. 100, 2017.

[36] N. N. Das, D. Entekhabi, E. G. Njoku, J. J. C. Shi, J. T. Johnson, and A. Colliander, "Tests of the SMAP combined radar and radiometer algorithm using airborne field campaign observations and simulated data," *IEEE Trans. Geosci. Remote Sens.*, vol. 52, no. 4, pp. 2018–2028, Apr. 2014.

[37] W. A. Fuller, *Measurement Error Models*, vol. 305. Hoboken, NJ, USA: Wiley, 2009.

[38] D. Entekhabi, N. Das, E. Njoku, J. Johnson, and J. Shi, "Algorithm theoretical basis document L2 & L3 radar/radiometer soil moisture (active/passive) data products," Jet Propuls. Lab., California Inst. Technol., Pasadena, CA, USA, Tech. Rep., 2014. [Online]. Available: https://smap.jpl.nasa.gov/system/internal_resources/details/original/277_L2_3_SM_AP_RevA_web.pdf

[39] J. J. W. Wilson *et al.*, "Radiometric calibration of the advanced wind scatterometer radar ASCAT carried onboard the METOP—A satellite," *IEEE Trans. Geosci. Remote Sens.*, vol. 48, no. 8, pp. 3236–3255, Aug. 2010.

[40] N. Das *et al.*, "Soil moisture active passive (SMAP) project assessment report for the L2SMSP beta-release data products," Jet Propuls. Lab., Calif. Inst. Technol., Pasadena, CA, USA Tech. Rep. JPL D-56549, 2017.

[41] Z. Bartalis, K. Scipal, and W. Wagner, "Azimuthal anisotropy of scatterometer measurements over land," *IEEE Trans. Geosci. Remote Sens.*, vol. 44, no. 8, pp. 2083–2092, Aug. 2006.

[42] M. Piles, J. Ballabrera-Poy, and J. Muñoz-Sabater, "Dominant features of global surface soil moisture variability observed by the SMOS satellite," *Remote Sens.*, vol. 11, no. 1, p. 95, Jan. 2019.

[43] J. S. Famiglietti, D. Ryu, A. A. Berg, M. Rodell, and T. J. Jackson, "Field observations of soil moisture variability across scales," *Water Resour. Res.*, vol. 44, no. 1, pp. 1–16, Jan. 2008, Art. no. W01423, doi: 10.1029/2006WR005804.

[44] D. J. Wilson, A. W. Western, and R. B. Grayson, "Identifying and quantifying sources of variability in temporal and spatial soil moisture observations," *Water Resour. Res.*, vol. 40, no. 2, pp. 1–10, Feb. 2004, Art. no. W02507, doi: 10.1029/2003WR002306.

[45] G. J. M. De Lannoy, N. E. C. Verhoest, P. R. Houser, T. J. Gish, and M. Van Meirvenne, "Spatial and temporal characteristics of soil moisture in an intensively monitored agricultural field (OPE3)," *J. Hydrol.*, vol. 331, nos. 3–4, pp. 719–730, Dec. 2006.

[46] M. Bracaglia, P. Ferrazzoli, and L. Guerriero, "A fully polarimetric multiple scattering model for crops," *Remote Sens. Environ.*, vol. 54, no. 3, pp. 170–179, Dec. 1995.

[47] P. Ferrazzoli and L. Guerriero, "Passive microwave remote sensing of forests: A model investigation," *IEEE Trans. Geosci. Remote Sens.*, vol. 34, no. 2, pp. 433–443, Mar. 1996.

[48] P. Ferrazzoli and L. Guerriero, "Radar sensitivity to tree geometry and woody volume: A model analysis," *IEEE Trans. Geosci. Remote Sens.*, vol. 33, no. 2, pp. 360–371, Mar. 1995.

[49] A. K. Fung, *Microwave Scattering and Emission Models and Their Applications*. Norwood, MA, USA: Artech House, 1994.

[50] M. A. Karam and A. K. Fung, "Electromagnetic scattering from a layer of finite length, randomly oriented, dielectric, circular cylinders over a rough interface with application to vegetation," *Int. J. Remote Sens.*, vol. 9, no. 6, pp. 1109–1134, Jun. 1988.

[51] H. J. Eom and A. K. Fung, "A scatter model for vegetation up to Ku-band," *Remote Sens. Environ.*, vol. 15, no. 3, pp. 185–200, Jun. 1984.

[52] H. J. Eom and A. K. Fung, "Scattering from a random layer embedded with dielectric needles," *Remote Sens. Environ.*, vol. 19, no. 2, pp. 139–149, Apr. 1986.

[53] D. M. LeVine, R. Meneghini, R. H. Lang, and S. S. Seker, "Scattering from arbitrarily oriented dielectric disks in the physical optics regime," *J. Opt. Soc. Amer.*, vol. 73, no. 10, pp. 1255–1262, 1983.

[54] L. Tsang, J. A. Kong, and K.-H. Ding, *Scattering of Electromagnetic Waves: Theories and Applications*, vol. 27. Hoboken, NJ, USA: Wiley, 2004.

[55] J.-P. Wigneron, A. Chanzy, J.-C. Calvet, and N. Bruguier, "A simple algorithm to retrieve soil moisture and vegetation biomass using passive microwave measurements over crop fields," *Remote Sens. Environ.*, vol. 51, no. 3, pp. 331–341, Mar. 1995.

[56] A. Chanzy, L. Guerriero, J.-P. Wigneron, and P. Ferrazzoli, "Multifrequency emission of wheat: Modeling and applications," *IEEE Trans. Geosci. Remote Sens.*, vol. 38, no. 6, pp. 2598–2607, 2000.

[57] A. Della Vecchia *et al.*, "Influence of geometrical factors on crop backscattering at C-band," *IEEE Trans. Geosci. Remote Sens.*, vol. 44, no. 4, pp. 778–790, Apr. 2006.

[58] C. Igathinathane, A. R. Womac, S. Sokhansanj, and L. O. Pordesimo, "Mass and moisture distribution in aboveground components of standing corn plants," *Trans. ASABE*, vol. 49, no. 1, pp. 97–106, 2006.

[59] P. Ferrazzoli, L. Guerriero, and J.-P. Wigneron, "Simulating L-band emission of forests in view of future satellite applications," *IEEE Trans. Geosci. Remote Sens.*, vol. 40, no. 12, pp. 2700–2708, Dec. 2002.

[60] A. D. Vecchia, K. Saleh, P. Ferrazzoli, L. Guerriero, and J.-P. Wigneron, "Simulating L-band emission of coniferous forests using a discrete model and a detailed geometrical representation," *IEEE Geosci. Remote Sens. Lett.*, vol. 3, no. 3, pp. 364–368, Jul. 2006.

[61] K. Saleh, A. Porte, D. Guyon, P. Ferrazzoli, and J.-P. Wigneron, "A forest geometric description of a maritime pine forest suitable for discrete microwave models," *IEEE Trans. Geosci. Remote Sens.*, vol. 43, no. 9, pp. 2024–2035, Sep. 2005.

[62] E. S. Kasischke, N. L. Christensen, and E. M. Haney, "Modeling of geometric properties of loblolly pine tree and stand characteristics for use in radar backscatter studies," *IEEE Trans. Geosci. Remote Sens.*, vol. 32, no. 4, pp. 800–822, Jul. 1994.

[63] F. Del Frate *et al.*, "Wheat cycle monitoring using radar data and a neural network trained by a model," *IEEE Trans. Geosci. Remote Sens.*, vol. 42, no. 1, pp. 35–44, Jan. 2004.

[64] M. Acuña, P. Ferrazzoli, and L. Guerriero, "Modeling L-and X-band backscattering of wheat and tests over fields of Pampas," *Eur. J. Remote Sens.*, vol. 52, pp. 84–101, Dec. 2019.

[65] S. Talebiesfandarani *et al.*, "Microwave vegetation index from multi-angular observations and its application in vegetation properties retrieval: Theoretical modelling," *Remote Sens.*, vol. 11, no. 6, p. 730, Mar. 2019.

[66] P. Ferrazzoli and L. Guerriero, "Interpretation and model analysis of MAESTRO 1 Flevoland data," *Int. J. Remote Sens.*, vol. 15, no. 14, pp. 2901–2915, Sep. 1994.

[67] A. Della Vecchia, P. Ferrazzoli, L. Guerriero, L. Ninivaggi, T. Strozzi, and U. Wegmuller, "Observing and modeling multifrequency scattering of maize during the whole growth cycle," *IEEE Trans. Geosci. Remote Sens.*, vol. 46, no. 11, pp. 3709–3718, Nov. 2008.

[68] V. Kalogirou, P. Ferrazzoli, A. Della Vecchia, and M. Foumelis, "On the SAR backscatter of burned forests: A model-based study in C-band, over burned pine canopies," *IEEE Trans. Geosci. Remote Sens.*, vol. 52, no. 10, pp. 6205–6215, Oct. 2014.

[69] P. Ferrazzoli, L. Guerriero, N. Pierdicca, and R. Rahmoune, "Forest biomass monitoring with GNSS-R: Theoretical simulations," *Adv. Space Res.*, vol. 47, no. 10, pp. 1823–1832, May 2011.

[70] A. Della Vecchia, P. Ferrazzoli, J.-P. Wigneron, and J. P. Grant, "Modeling forest emissivity at L-band and a comparison with multitemporal measurements," *IEEE Geosci. Remote Sens. Lett.*, vol. 4, no. 4, pp. 508–512, Oct. 2007.

[71] A. Della Vecchia *et al.*, "Modeling the multifrequency emission of broadleaf forests and their components," *IEEE Trans. Geosci. Remote Sens.*, vol. 48, no. 1, pp. 260–272, Jan. 2010.

[72] V. L. Mironov, L. G. Kosolapova, and S. V. Fomin, "Physically and mineralogically based spectroscopic dielectric model for moist soils," *IEEE Trans. Geosci. Remote Sens.*, vol. 47, no. 7, pp. 2059–2070, Jul. 2009.

[73] P. O'Neill, S. Chan, E. Njoku, T. Jackson, and R. Bindlish, "SMAP L3 radiometer global daily 36 km EASE-grid soil moisture, version 6," in *Proc. NASA Nat. Snow Ice Data Center Distrib. Active Arch. Center*, 2019. Accessed: Oct. 2019, doi: 10.5067/EVYDQ32FNWTH.

[74] J. Figa-Saldaña, J. J. W. Wilson, E. Attema, R. Gelsthorpe, M. R. Drinkwater, and A. Stoffelen, "The Advanced Scatterometer (ASCAT) on the meteorological operational (MetOp) platform: A follow on for European wind scatterometers," *Can. J. Remote Sens.*, vol. 28, no. 3, pp. 404–412, Jan. 2002.

[75] D. Entekhabi, N. Das, E. Njoku, T. Jackson, and J. Shi, "SMAP L3 radar/radiometer global daily 9 km EASE-grid soil moisture, version 3," in *Proc. NASA Nat. Snow Ice Data Center Distrib. Active Arch. Center*, 2016. Accessed: Oct. 2019.

[76] H. Saf, "Metop ASCAT surface soil moisture climate data record v5 12.5 km sampling (H115)," EUMETSAT SAF Support Oper. Hydrol. Water Manage., Tech. Rep., 2019, doi: 10.15770/EUM_SAF_H_0006.

[77] P. O'Neill, S. Chan, E. Njoku, T. Jackson, and R. Bindlish, "SMAP L2 radiometer half-orbit 36 km EASE-grid soil moisture," in *Distributed Active Archive Center Version 4*. Boulder, CO, USA: Colo NASA National Snow and Ice Data Center, 2016.

[78] M. J. Baur, T. Jagdhuber, A. F. Feldman, R. Akbar, and D. Entekhabi, "Estimation of relative canopy absorption and scattering at L-, C- and X-bands," *Remote Sens. Environ.*, vol. 233, Nov. 2019, Art. no. 111384.

[79] M. Link, M. Drusch, and K. Scipal, "Soil moisture information content in SMOS, SMAP, AMSR2, and ASCAT level-1 data over selected *in situ* sites," *IEEE Geosci. Remote Sens. Lett.*, vol. 17, no. 7, pp. 1213–1217, Jul. 2020.

[80] Y. Du, F. T. Ulaby, and M. C. Dobson, "Sensitivity to soil moisture by active and passive microwave sensors," *IEEE Trans. Geosci. Remote Sens.*, vol. 38, no. 1, pp. 105–114, 2000.

[81] H. Huang, L. Tsang, E. G. Njoku, A. Colliander, T.-H. Liao, and K.-H. Ding, "Propagation and scattering by a layer of randomly distributed dielectric cylinders using Monte Carlo simulations of 3D Maxwell equations with applications in microwave interactions with vegetation," *IEEE Access*, vol. 5, pp. 11985–12003, 2017.

[82] H. Huang and L. A. S. Tsang Colliander Yueh, "Propagation of waves in randomly distributed cylinders using three-dimensional vector cylindrical wave expansions in Foldy–Lax equations," *IEEE J. Multiscale Multiphys. Comput. Techn.*, vol. 4, pp. 214–226, 2019.

Moritz Link received the B.S. degree in physical geography and the M.S. degree in environmental systems and sustainability from the Ludwig-Maximilians-Universität, Munich, Germany, in 2014 and 2017, respectively.

From 2016 to 2017, he was a Visiting Student with the Department of Civil and Environmental Engineering, Massachusetts Institute of Technology (MIT), Cambridge, MA, USA. He was also with the Microwaves and Radar Institute, German Aerospace Center (DLR), Oberpfaffenhofen, Germany, and the Earth and Mission Science Division, European Space Agency (ESA), Noordwijk, the Netherlands. His research interests include active and passive microwave remote sensing over land.

Thomas Jagdhuber (Senior Member, IEEE) received the Diploma degree in physical geography, physics, remote sensing, and geoinformatics from Ludwig Maximilian University (LMU) and Technical University (TUM) of Munich, Munich, Germany, in 2006 and the Ph.D. degree in hydrology from the Faculty of Science, University of Potsdam, Potsdam, Germany, in 2012.

From 2014 through 2019, he was a yearly Visiting Scientist with the Massachusetts Institute of Technology (MIT), Boston, MA, USA, contributing to the preparation and continuation of the Soil Moisture Active and Passive (SMAP) and SMAP/Sentinel-1 missions. In addition, he serves as a Lecturer for the University of Jena, Jena, Germany, and the University of Augsburg, Augsburg, Germany, where he is also affiliated with the Institute of Geography at the faculty of computer science as a habilitation candidate. His main research interests include physics-based multisensor data integration with a focus on active and passive microwave interaction theory and on polarimetric techniques for hydrological, agricultural, ecological, and cryospheric parameter modeling and estimation. He is also interested in the coupling of multisensor remote sensing with earth system modeling for joint parameter retrieval and mutual validation. Since 2007, he is affiliated with the Microwaves and Radar Institute (HR) of the German Aerospace Center (DLR).

Dr. Jagdhuber was honored with the DLR Science Award for his research on polarimetric synthetic aperture radar (SAR) decomposition techniques in 2014. Together with Prof. Dr. Entekhabi (MIT), he was awarded the MIT-MISTI grant for global water cycle and environmental monitoring using active and passive satellite-based microwave instruments. In addition, he is a reviewer for several international journals and conference boards.

Paolo Ferrazzoli (Senior Member, IEEE) graduated from the University "La Sapienza" of Rome, Rome, Italy, in 1972.

In 1974, he joined Telespazio s.p.a., Rome, where he was mainly active in the fields of antennas, slant-path propagation, and advanced satellite telecommunication systems. In 1984, he joined Tor Vergata University of Rome, Rome, where he teached microwaves, radiowave propagation, and electromagnetic fields. His research was focused on microwave remote sensing of vegetated terrains, with particular emphasis on electromagnetic modeling. He was involved in international experimental remote sensing campaigns such as AGRISAR, AGRISCATT, MAESTRO-1, MAC-Europe, and SIR-C/X-SAR. He participated in the coordinating team of the ERA-ORA Project, funded by EEC, establishing an assemblage among several European researchers working in radar applications.

Mr. Ferrazzoli was a member of Science Advisory Group and a member of Quality Working Group in the framework of the European Space Agency (ESA) SMOS Project. He was Chair of MICRORAD 2012 International Meeting, and a member of the Technical Program Committee of IGARSS Conferences from 2012 to 2018.

Leila Guerriero (Member, IEEE) received the Laurea degree in physics from the Sapienza University of Rome, Rome, Italy, in 1986 and the Ph.D. degree in electromagnetism from the Tor Vergata University of Rome, Rome, in 1991.

Since 1994, she has been a Permanent Researcher with Tor Vergata University, where she is an Associate Professor holding the courses on Earth Satellite Observation and on Geoinformation. Her research interests include modeling microwave scattering and emissivity from agricultural and forested areas. She participated in several international projects, among them: the European Space Agency (ESA) projects Soil Moisture and Ocean Salinity Satellite, Development of synthetic aperture radar (SAR) Inversion Algorithms for Land Applications, Use of Bistatic Microwave Measurements for Earth Observation, and SAOCOM-CS Bistatic Imaging, Radiometry and Interferometry Over Land. Lately, she has been involved in the modeling of Global Navigation Satellite System Reflectometry (GNSS-R) signals for ESA projects and in the European FP7 and H2020 Programmes.

Dr. Guerriero is a member of the Permanent Steering Scientific Committee of MicroRad. She is Secretary and Treasurer of the GRSS North-Central Italy Chapter.

Dara Entekhabi (Fellow, IEEE) received the B.S. and M.S. degrees in geography from Clark University, Worcester, MA, USA, in 1983 and 1985, 1988, respectively, and the Ph.D. degree in civil and environmental engineering from the Massachusetts Institute of Technology (MIT), Cambridge, MA, in 1990.

He is a Professor with the Department of Civil and Environmental Engineering and the Department of Earth, Atmospheric and Planetary Sciences, MIT. He is the Science Team Lead for the National Aeronautics and Space Administration's Soil Moisture Active and Passive (SMAP) mission that was launched on January 31, 2015. His research includes terrestrial remote sensing, data assimilation, and coupled land–atmosphere systems modeling.

Dr. Entekhabi is also a Fellow of the American Meteorological Society and the American Geophysical Union. He is a member of the National Academy of Engineering.